



## Impact of partial echo on 4D flow MRI: the insight from synthetic MRI

Morgane Garreau, Thomas Puiseux, Ramiro Moreno, Solenn Toupin, Daniel Giese, Franck Nicoud, Simon Mendez

### ► To cite this version:

Morgane Garreau, Thomas Puiseux, Ramiro Moreno, Solenn Toupin, Daniel Giese, et al.. Impact of partial echo on 4D flow MRI: the insight from synthetic MRI. 2026. hal-05449296

HAL Id: hal-05449296

<https://hal.science/hal-05449296v1>

Preprint submitted on 8 Jan 2026

**HAL** is a multi-disciplinary open access archive for the deposit and dissemination of scientific research documents, whether they are published or not. The documents may come from teaching and research institutions in France or abroad, or from public or private research centers.

L'archive ouverte pluridisciplinaire **HAL**, est destinée au dépôt et à la diffusion de documents scientifiques de niveau recherche, publiés ou non, émanant des établissements d'enseignement et de recherche français ou étrangers, des laboratoires publics ou privés.



Distributed under a Creative Commons CC BY-ND 4.0 - Attribution - No Derivative Works - International License

# Impact of partial echo on 4D flow MRI: the insight from synthetic MRI

Morgane Garreau<sup>1,2,3</sup> | Thomas Puiseux<sup>2,4</sup> | Ramiro Moreno<sup>4,5</sup> | Solenn Toupin<sup>6</sup> | Daniel Giese<sup>7</sup> | Franck Nicoud<sup>1,8</sup> | Simon Mendez<sup>1</sup>

<sup>1</sup>IMAG, Univ. Montpellier, CNRS, Montpellier, France

<sup>2</sup>Spin Up, ALARA Group, Strasbourg, France

<sup>3</sup>INRIA Saclay, Palaiseau, France

<sup>4</sup>I2MC, INSERM/UPS UMR 1297, Toulouse, France

<sup>5</sup>ALARA Expertise, ALARA Group, Strasbourg, France

<sup>6</sup>Siemens Healthineers France, Saint-Denis, France

<sup>7</sup>Research & Clinical Translation, Magnetic Resonance, Siemens Healthineers AG, Erlangen, Germany

<sup>8</sup>Institut Universitaire de France, Paris, France

## Correspondence

Franck Nicoud, University of Montpellier, CNRS, Montpellier, France. Email: franck.nicoud@umontpellier.fr

## Present Address

## Funding Information

GENCI-CINES, Grant Numbers: A0120312498 and A0140312498; MESO@LR-Platform - University of Montpellier; Spin Up

## Abstract

**Purpose:** The aim of this study is to investigate the impact of the partial echo on 4D flow MRI sequences thanks to in silico coupled MRI-CFD (Computational Fluid Dynamics) simulations.

**Methods:** Two sequences are studied: one with a full echo (FE) and another using partial echo (PE) with an echo symmetry fraction of 0.75. MRI-CFD simulations are conducted on an in silico pulsatile flow phantom for a sinusoidal inflow and a physiological inflow typical of the ascending aorta.

**Results:** For both inflow signals, PE-based simulations exhibited better compliance with their matching CFD simulations compared to the FE ones.

**Conclusion:** The reduction of flow misregistration artifacts achieved through the use of PE appears to be more beneficial than the drawback of incomplete k-space filling. The MRI-CFD framework presented in this study appears as a useful tool to investigate the design of MRI sequences and to stratify its different sources of errors.

## KEYWORDS:

4D flow, partial echo (PE), computational fluid dynamics (CFD), numerical simulation

**WORD COUNT:** 4998

## 1 | INTRODUCTION

Time-resolved 3D phase-contrast MRI (PC-MRI), also known as 4D flow MRI, is a growing modality to evaluate hemodynamics. It gives access to quantification of blood flow dynamics inside a volume of interest over the cardiac cycle. As noted in the 2023 updated consensus paper on the topic<sup>1</sup>, 4D flow MRI is at a turning point to

become clinically available. This is explained by substantial progress in the field, particularly in the development of acceleration methods and acquisition strategies to reduce scan times to 5-10 minutes. Furthermore, 4D flow MRI sequences have become available on clinical MRI scanners from major vendors. However, its accuracy and reliability depends on various decisions such as the choice of sequences, acquisition parameters or postprocessing techniques. Clear guidelines appear as essential for clinicians to introduce 4D flow MRI in their daily practice.

**Abbreviations:** PF, partial Fourier; PE, partial echo; FE, full echo;  $T_D$ , displacement time; CFD, computational fluid dynamics; PC, phase-contrast

The most common acquisition strategy is the Cartesian scheme, with a single line of k-space acquired for each repetition time. Instead of collecting the entire k-space, some methods acquire only a subset of it. One of them, called partial Fourier (PF), is a technique where the data is not collected symmetrically: one half of the k-space is completely filled, while only a small amount of the other half is. Several algorithms have been proposed to reconstruct the MR images from these undersampled k-spaces. The most common are zero-filling, homodyne processing, or POCS algorithm<sup>2,3,4,5</sup>.

When PF is used along the phase- and/or slice-encoding direction, the main goal is to reduce scan time. On the other hand, PF along the frequency-direction, also known as asymmetric or partial echo (PE), mainly aims to reduce  $T_E$ . PE is widely used in angiographic and cardiac applications in order to reduce flow and motion errors<sup>2</sup>. These errors, known as misregistration artifacts, happen whenever the moving spins change position between phase- and frequency-encoding. In PC-MRI, this translates to mapping the correct velocities to incorrect spatial locations<sup>6</sup> when velocity-encoding and phase-encoding are synchronized. Flow-compensation can be used to eliminate these artifacts in MR angiography by nulling the first gradient moment, but do not compensate for higher-order motion (e.g., acceleration, jerk)<sup>7</sup>. Another aspect of misregistration is velocity displacement artifacts. They occur because of the acceleration of spins during spatial and velocity encodings and lead to incorrect velocities assigned to the spatial locations. The misregistration artifacts can be mitigated by synchronizing the spatial and velocity encodings. In conventional Cartesian 4D flow MRI, this synchronization is possible except along the frequency-encoding direction, since the velocity encoding must occur before the readout<sup>8</sup>.

An illustration of the impact of PE on an MRI sequence is presented in Figure 1. Note that this illustration is intended for pedagogical purposes. In the sequences used in this study (see Section 2.1), the bipolar and the readout prephaser gradients are merged, but they are shown separately in Figure 1 for clarity. In full echo (FE, Figure 1 (a)), the echo time matches the center of the readout gradient. PE aims at creating an echo before reaching this time point. Thereby, it consists in reducing the strength and/or duration of the pre-phasing gradient (cf. Figure 1 (c) vs. Figure 1 (b)). This contributes to a reduction of all gradient moments, in particular of the high-order flow artifacts (e.g., acceleration, jerk) when flow-compensation is used<sup>7</sup>. This also mitigates the signal loss in disturbed flows<sup>10,7</sup>. Note that, beyond shortening  $T_E$ , it also reduces the displacement time  $T_D$  along the readout axis.  $T_D$  represents the time

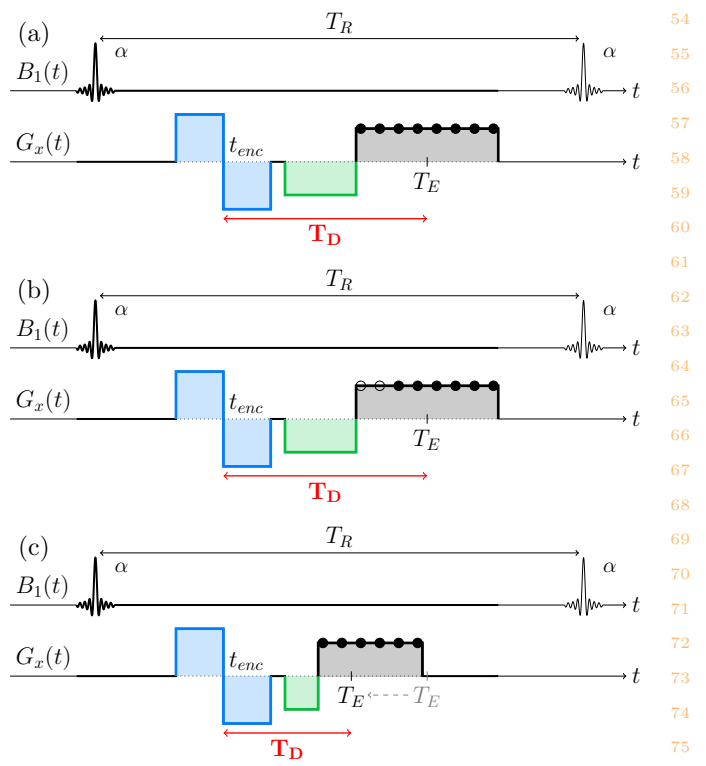


**FIGURE 1** Illustration of (a) full echo acquisition against (b) partial echo one. (c) represents how partial echo reduces the displacement time  $T_D$ . Filled circles represent acquired time instants and dotted circles non-acquired data points. Only the radiofrequency  $B_1$  and the gradients along the readout direction  $G_x$  are represented for simplification. The bipolar gradient to encode the velocity is highlighted in blue, the prephaser in green and the readout in gray. Note that the time delay between the bipolar gradient and the prephaser could be reduced, and even both gradients could be merged as long as the expected gradient moments<sup>9</sup> are conserved (e.g., same area under the gradient waveform). They are not merged in this illustration for clarity. No other gradient can be merged with the readout one in conventional Cartesian sampling as it would induce a shift in the k-space.

delay between the effective encoding time  $t_{enc}$  and the spatial encoding time, where  $t_{enc}$  corresponds to the time instant when the sensitivity  $S_2$  cancels out (cf. Equation 1)<sup>11,6,8</sup>. By definition, the spatial encoding time along the frequency encoding direction is  $T_E$ . Along the two phase encoding directions,  $T_D$  can be nullified thanks to the synchronization between the velocity and spatial encoding gradients. Thereby the terms  $t_{enc}$  and  $T_D$  in the following will only refer to the frequency-encoding direction.

Overall, PE contributes to the reduction of misregistration artifacts. Yet, it leads to an undersampled k-space, and possible errors in the reconstructed velocity fields<sup>12</sup>. The present work examines whether the use of PE should be recommended in the context of 4D Flow

MRI. Is PE beneficial to the reconstructed velocity fields by diminishing the flow artifacts, or is it instead detrimental due to the partial sampling of k-space and the associated challenges in reconstructing the missing data? Reference data is lacking to answer these questions.

Over the past years, simulation of MRI sequences has emerged as a useful tool to develop and optimize pulse sequences. Several methods specific to PC-MRI simulations have been proposed in the literature. To name a few, Steinman *et al.* have simulated spatial and velocity displacement artifacts occurring in a 2D and a 3D PC-MRI sequence on an anastomosis geometry<sup>6</sup>. More recently, Weine *et al.* have developed a Python package to simulate cardiovascular MR images, which can deal with complex motion and flow<sup>13</sup>. Among other examples, they have simulated PC-MRI of a turbulent flow in a stenosis. These different frameworks and their validation against experimental acquisitions show the feasibility and potential of simulating synthetic PC-MRI images. Beyond validation, numerical simulations have also been used to investigate differences between various sequences. In particular, Klepaczko *et al.* have developed a numerical framework to simulate different MR angiography protocols<sup>14</sup>. They have applied their method to evaluate an accelerated 2D PC-MRI with an EPI readout against conventional 2D and 3D PC-MRI sequences, in the context of renal circulation<sup>14,15</sup>.

In this work, the impact of PE on 4D flow MRI sequences is investigated in the light of MR simulations coupled with computational fluid dynamics (CFD). The simulations are conducted in the in-house pulsatile flow phantom geometry introduced by Puiseux *et al.*<sup>16,17</sup> and shown in Figure 2. Two distinct flow regimes are prescribed at the inlet. The first signal corresponds to an experimentally measured, nearly sinusoidal flow rate<sup>18</sup>. The second is defined using a function representative of an aortic flow rate<sup>19</sup>. Two realistic vendor 4D flow MRI sequences are investigated: one with FE and the other with PE.

## 2 | METHODS

### 2.1 | Sequence design

The 4D flow MRI research sequences used in this work have been provided by Siemens Healthineers, as the goal of the present study is to evaluate realistic sequences. Using the POET sequence simulation tool (Siemens Healthineers, Erlangen, Germany), one can adapt the sequence parameters, simulate the sequence, and extract

the gradient and radiofrequency diagrams. The parameters of the two sequences are summarized in Table 1.

**TABLE 1** Sequence parameters.

<i>Partial echo (PE)</i>	No	Yes	60
<i>Echo symmetry fraction (ESF)</i>	1.0	0.75	61
<i>FOV (mm<sup>3</sup>)</i>	136 × 56 × 192		62
<i>Acquired voxel size (mm<sup>3</sup>)</i>	2 × 2 × 2		63
<i>Flip angle (°)</i>	7		64
<i>Readout bandwidth (Hz/voxel)</i>	560		65
<i>Velocity encoding V<sub>ENC</sub> (x, y, z; cm/s)</i>	70-20-70		66
<i>T<sub>E</sub> (ms)</i>	4.20	4.16	66
<i>T<sub>R</sub> (ms)</i>	6.52	6.49	67
<i>Temporal resolution (ms)</i>	52.16	52.20	68
<i>Number of acquired cardiac phases</i>	17		69
<i>Cardiac period (s)<sup>a</sup></i>	1.01712	1.01860	70
<i>Displacement time T<sub>D</sub> (ms)<sup>a,b</sup></i>	1.99	1.52	71

<sup>a</sup>The cardiac period and the displacement time can not be directly specified in IDEA. <sup>b</sup>T<sub>D</sub> has been computed once the sequence had been generated.

The parameters are chosen to match the experimental parameters used in a former study on the in-house phantom, where accelerated sequences of 4D flow MRI have been compared to a fully-sampled sequence and CFD simulations<sup>18</sup>. The virtual acquisition is made in the coronal orientation: the readout, phase-encoding and slice-selecting directions corresponds to the Z, X and Y axes in the scanner reference frame, respectively. The voxels are isotropic (2 mm<sup>3</sup>). The V<sub>ENC</sub> is set to 70 cm/s for the in-plane velocities (along X and Z) and 20 cm/s for the through-plane velocity.

The dimensions of the FOV have been chosen up to the limit where aliasing would occur, hence reducing the simulation time. The size of the FOV with respect to the phantom mesh is presented in Figure 2. Note that the Z-dimension is significantly larger than the object because of the default two-fold oversampling in this direction.

The temporal parameters have been adjusted in order to achieve a cardiac cycle duration close to 1 s for both sequences. A prospective gating has been chosen over a retrospective one, because it has been found to be more flexible to control the number of acquired cardiac phases. Even with this versatility, an uncontrollable and irreducible time delay exists between two successive cardiac cycles. This built-in parameter is likely due to the fact that if the sequence were to be used experimentally, the acquisition would stop after collecting the required number of cardiac phases and wait to be triggered by the next desired physiological event (e.g., next R-wave).

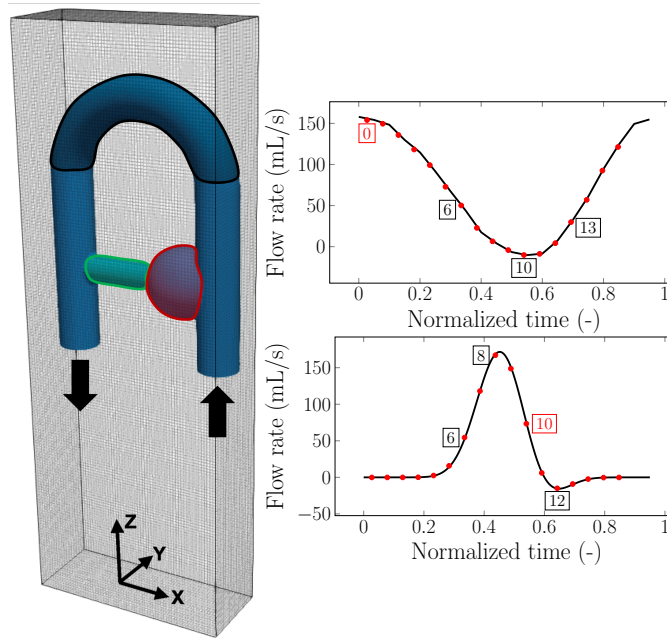


**FIGURE 2** Field-of-view, phantom and flow rates. On the left-hand side, the FOV and the phantom mesh are depicted. The inlet and outlet are indicated by the arrows. Main geometric features of the phantom are highlighted: the aneurysm-like region in red, the collateral in green and the U-bend in darker blue. On the right, the two studied flow regimes used as input to the computational fluid dynamics simulations are drawn in black: above the sinusoidal flow rate from experimental data<sup>18</sup> and below the physiological flow rate (cf. Eq. (2)). The red dots correspond to the averaged time of each cardiac phase. In the following figures, the focus is set on the phases indicated with red numbers (phase 0 for the sinusoidal inflow and phase 10 for the physiological inflow). The figures corresponding to the phases whose numbers are indicated in black are provided as Supporting Information.

The FE sequence is first designed with all the considerations made so far and with the minimal  $T_E$  and  $T_R$ . An interleaved symmetric 4-point velocity-encoding scheme is selected<sup>20,21</sup>. This corresponds to the successive acquisition of the same phase-encoding line, yet with four different combinations of velocity-encoding gradients. Two segments per velocity-encoding direction are collected in each cardiac phase (i.e.,  $2 \times 4 = 8$  segments) and 17 cardiac phases are acquired per cycle.

The second sequence is set to present an echo symmetry fraction of 75%. This corresponds to sampling only half of the negative  $k$  frequencies and all of the positive ones. In order to compare the two sequences and to acquire the same number of cardiac phases, the same  $T_R$  is chosen, but the  $T_E$  is reduced to the minimal value available. A shorter  $T_R$  could be achieved for this sequence. This could eventually allow to acquire a

higher number of cardiac phases, thereby improving the temporal resolution. Recall that this study focuses on PF along the frequency-direction. No reduction of scan time is expected as opposed to sequences using PF along the phase-encoding direction(s), which would require less repetitions. The small difference of  $T_R$  values between the two sequences reported in Table 1 is due to rounding effects. Concerning the temporal resolution, the small deviation is likely due to the time delays mentioned previously.

In the context of flow MRI, an additional relevant time parameter is  $T_D$ . It can be defined as the total duration over which the spatial- and velocity-encodings occur<sup>6</sup>. In the sequences investigated here, the spatial encoding along the two phase directions and all velocity encodings are synchronized<sup>8</sup> by merging the bipolar and the phase-encoding gradients. Moreover, the readout prephaser gradient is also merged with the bipolar gradient along the frequency encoding direction. However, the spatial encoding along this direction occurs during the readout gradient after all other gradients have been played. The effective encoding time  $t_{enc}$  can be estimated as the time instant when the sensitivity  $S_2$  cancels out<sup>6,11</sup>, where the sensitivities  $S_n$  are defined as:

$$S_n = \frac{\gamma}{n!} \int_{t_0}^{T_E} \Delta G(t)(t - t_{enc})^n dt. \quad (1)$$

$t_0$  denotes the center of the RF pulse and  $\Delta G(t)$  is the difference in gradients between the positive and negative velocity encoding lobes associated with the velocity component  $w$  encoded along the readout direction (the other directions are not considered thanks to synchronization).  $T_D$  along this direction is then computed as the delay between  $t_{enc}$  and  $T_E$ . It equals 1.99 ms for FE and reduces to 1.52 ms for PE. While PE resulted in a reduction of about 1% in  $T_E$ , the reduction in  $T_D$  is found to be close to 25%.

## 2.2 | MRI-CFD simulations

The simulations were carried out using the MRI-CFD framework introduced by Puiseux et al.<sup>17</sup> and implemented in the in-house YALES2BIO software<sup>22</sup>. The fluid is modeled as incompressible and Newtonian with the following characteristics:  $\nu = 4.02 \times 10^{-6} \text{ m}^2/\text{s}$ ,  $\rho = 1020 \text{ kg/m}^3$ ,  $T_1 = 0.85 \text{ s}$  and  $T_2 = 0.17 \text{ s}$  at 1.5 T, matching the experimental setup used in<sup>18</sup>. The tetrahedral-based mesh of the phantom, generated in Gambit 2.4.6 (ANSYS, Inc., Canonsburg, PA), has a characteristic cell size of 2 mm. Eight particles are seeded per mesh cell, resulting in an initial spin density of 48 particles/voxel to keep a reasonable computing time. The

computational domain is presented on the left side of Figure 2 .

Two pulsatile flow regimes are studied. The first follows the experimental flow rate presented in<sup>18</sup>, yet dilated to match the cardiac periods. From now on, this flow rate is referred to as *sinusoidal*, since its shape is close to a sine wave. The second investigated flow is derived from a mathematical function modelling the flow into the ascending aorta<sup>19</sup>. The flow rate  $Q$  is governed by the following equation:

$$Q(t) = Q_0 \sin^n(\omega t) \cos(\omega t - \phi) \quad (2)$$

where  $\omega = \frac{\pi}{T_c}$ ,  $T_c$  the period of the cardiac cycle,  $n = 13$  and  $\phi = \frac{\pi}{10}$  as determined by Stevens et al<sup>19</sup>.  $Q_0$  is a multiplying factor, here tuned to achieve a maximal flow rate comparable to the sinusoidal flow rate. This minimizes the probabilities to produce velocities higher than the  $V_{ENC}$ . This second flow regime is subsequently referred to as *physiological* for the sake of simplicity. Yet, it is not a patient-specific inflow, but rather an analytical model reproducing physiological characteristics. Both flow rates are presented in Figure 2 .

The use of idealized spatial velocity profiles as inlet boundary conditions has been reported to negatively impact the CFD solution<sup>23</sup>. Hence, one would like to prescribe experimental data instead. Here, experimental data are only available for the sinusoidal flow rate, giving access to pixel-based velocity fields. In order to use the same pre-processing method for both inflows, an averaged normalized velocity field at the inlet is computed. This field corresponds to the time-average of the 20 experimentally acquired phases from the non-accelerated sequence presented in<sup>18</sup> normalized by their flow rate. This inlet velocity field is then multiplied by the sinusoidal and the physiological flow rates, respectively, and the shape of the velocity profile is the same throughout the cardiac cycle.

In total, four simulations are conducted, that is for both flow rates with and without PE. For each simulation, 40 cycles are first run without the coupling with the MRI sequence. The first 10 cycles allow to evacuate the effect of the initial conditions. The following 30 cycles are for phase-averaging purposes. More details about the CFD simulations can be found in<sup>16,18</sup>. The last cycle of each CFD simulation is used as initial condition to the MRI-CFD coupled simulations. The MRI-CFD simulation procedure uses a Eulerian-Lagrangian approach. The fluid flow is solved with the Navier-Stokes equations. Massless tracers, representing isochromats, are seeded uniformly in the phantom at the beginning of each RF excitation. The local fluid velocity field is interpolated and the Bloch equations are solved on these tracers. A perfect spoiling is performed by reinitializing all particles

at the end of each repetition time. More details about the numerical method can be found in<sup>17</sup>.

## 2.3 | Post-processing

The output of the MRI-CFD simulations is a synthetic MR signal. Magnitude and velocity images for each cardiac phase are reconstructed with in-house Python scripts. For the PE acquisitions, the k-space is zero-filled. While more sophisticated reconstructions of missing k-space frequencies exist, they generally rely on the assumption of Hermitian symmetry of the k-space and of smooth spatial variation of the phase to estimate the phase images. Hence, these methods do not preserve phase information and are not suitable for phase-contrast imaging<sup>2,24</sup>. Lower noise levels have been reported when reconstructing 4D flow MRI data with zero-filling in contrast to the more complex homodyne reconstruction and POCS algorithm<sup>25</sup>. Additionally, *artificial* PE reconstructions have been created based on each FE acquisition, where the k-space frequencies corresponding to the missing ones in the PE acquisitions have been artificially set to zero. The synthetic MRI images are then reconstructed in the same manner as for the PE acquisitions. Such *artificial* PE was performed to separate the effect of zero-filling the k-space (PE and *artificial* PE vs FE) from the effect of reducing  $T_D$  (PE vs FE and *artificial* PE). Finally, no gradient field distortions are modeled in the simulations, hence no background phase correction is required.

The CFD simulations used to compare with the synthetic MRI images are the ones simulated before the coupled MRI-CFD simulations. From now on, all CFD velocity maps presented refer to the downsampled velocity fields, which have been phase-averaged at the times of the corresponding cardiac phases. More details about the phase-averaging and downsampling processes can be found in<sup>16,18</sup>.

## 2.4 | Comparison methods

The synthetic MRI without and with the use of PE are compared with each other, and with their corresponding CFD simulation. To qualitatively compare all modalities, the synthetic MRI images are masked to cancel out the voxels outside the fluid domain. This is done using a binary mask based on the phase-averaged and downsampled CFD velocity fields averaged over the cardiac phases. The root mean square error (RMSE) is computed as follows. In order to compare the four synthetic MRI, the normalization is made with respect to the highest expected velocity, that is  $\max(V_{ENC}) = 0.7$  m/s. For

two fields A and B, it reads:

$$RMSE(\vec{x}, t) = \frac{\sqrt{(u_A - u_B)^2 + (v_A - v_B)^2 + (w_A - w_B)^2}}{\max(V_{ENC})} \quad (3)$$

where  $\vec{u} = (u, v, w)$  is the velocity vector associated to the node at the position  $\vec{x}$  ( $u$  is the velocity component along the X-axis,  $v$  along the Y-axis and  $w$  along the Z-axis, cf. Figure 2). The normalized absolute velocity difference along each direction is computed using the same normalization.

## 2.5 | Metrics to investigate the sources of errors

The discrepancies observed between CFD and synthetic MRI can occur from various sources or phenomena, such as the acceleration, the turbulence, or the multiple encoding times inherent to the image acquisition process. Acceleration-induced artifacts due to the time delay between velocity and spatial encoding have been reported in the literature<sup>11,6</sup>. As for turbulence, signal loss and consequent flow errors have been observed in stenotic jets<sup>26,27</sup>.

During the CFD simulation, the acceleration is computed as follows:

$$\frac{D\vec{u}}{Dt} = \frac{\partial \vec{u}}{\partial t} + (\vec{u} \cdot \nabla) \vec{u} \quad (4)$$

where the first term on the right-hand side corresponds to the partial time derivative and the second is induced by velocities heterogeneities. The first term is computed using a first-order upwind finite difference scheme and the second one using a 4th-order finite volume scheme. The (total) acceleration field is phase-averaged in the same manner as the velocity field.

The instantaneous velocity field computed during the simulation can be seen as the sum of the phase-averaged velocity  $\bar{u}$  and of an additional fluctuating part  $u'$ . The resolved turbulent kinetic energy (TKE) can then be computed as

$$TKE(\vec{x}, t) = \frac{1}{2} \left( \bar{u'^2}(\vec{x}, t) + \bar{v'^2}(\vec{x}, t) + \bar{w'^2}(\vec{x}, t) \right) \quad (5)$$

where  $\bar{\cdot}$  stands for the phase-averaging. 4D flow MRI do not give direct access to the fluctuating velocity field. Yet, this component exists in the flows typical of the large arteries with flow regimes at the laminar-turbulent transition. Such flows lead to intravoxel dephasing and consequently to a local loss of signal magnitude<sup>27,7</sup>. TKE is used as a proxy for the intravoxel velocity standard deviations as defined in<sup>28</sup>. Maps of acceleration of the fluid elements and of the TKE will be displayed along with patterns of the RMSE between the CFD and the

synthetic MRI simulations, without and with the use of PE.

## 3 | RESULTS

### 3.1 | Flow structure

The velocity maps for phase 0 of the sinusoidal flow rate and for phase 10 of the physiological flow rate are shown in Figure 3 and Figure 4, respectively. As highlighted in Figure 2 by the phase numbers in red, phase 0 corresponds to the highest flow rate of the sinusoidal inflow and phase 10 to the highest deceleration of the physiological inflow. The velocity maps corresponding to the other phases indicated in black in Figure 2 are provided as Supporting Information Figures S1-6. Recall that two CFD simulations are performed to meet the slightly different parameters of the sequences with and without PE. The errors between synthetic MRI and CFD presented afterwards are computed with respect to the matching CFD. However, as both simulations are very close to one another, only the CFD corresponding to the acquisition with PE are presented in Figures 3 and 4. Overall, the main flow structure is well represented by synthetic MRI without and with the use of PE. Despite the downsampling performed on the CFD, the synthetic MRI velocity fields appear blurrier than the CFD ones. Some discrepancies can already be noticed such as in the collateral for phase 0 (circled region in Figure 3) where darkened spots are observed or in the aneurysm-like region (circled region in Figure 2) for phase 10.

### 3.2 | Impact of the use of partial echo

To quantify the differences when using PE or not, the normalized absolute differences and the RMSE are computed. First, the evolution of the errors over time for FE and PE are displayed in Figure 5 for the sinusoidal and for the physiological flow rates, respectively. A Wilcoxon signed-rank test is conducted for each flow rate to determine whether there is a statistically significant difference between the RMSE obtained for FE and for PE across the cardiac phases. The test reveals a significant difference for both inflows ( $z = 3.0$ ,  $p < 0.0001$  for the sinusoidal one and  $z = 0.0$ ,  $p < 0.0001$  for the physiological one) with large effect size ( $|r| = 0.84$  for the sinusoidal inflow and  $|r| = 0.88$  for the physiological one). For both flows, the lowest levels of errors are found for the sequence with PE (dashed lines), with the exception of phase 13 of the sinusoidal flow. Apart from this phase, the RMSE when using PE (black dashed lines) is consistently below the RMSE without using PE (black

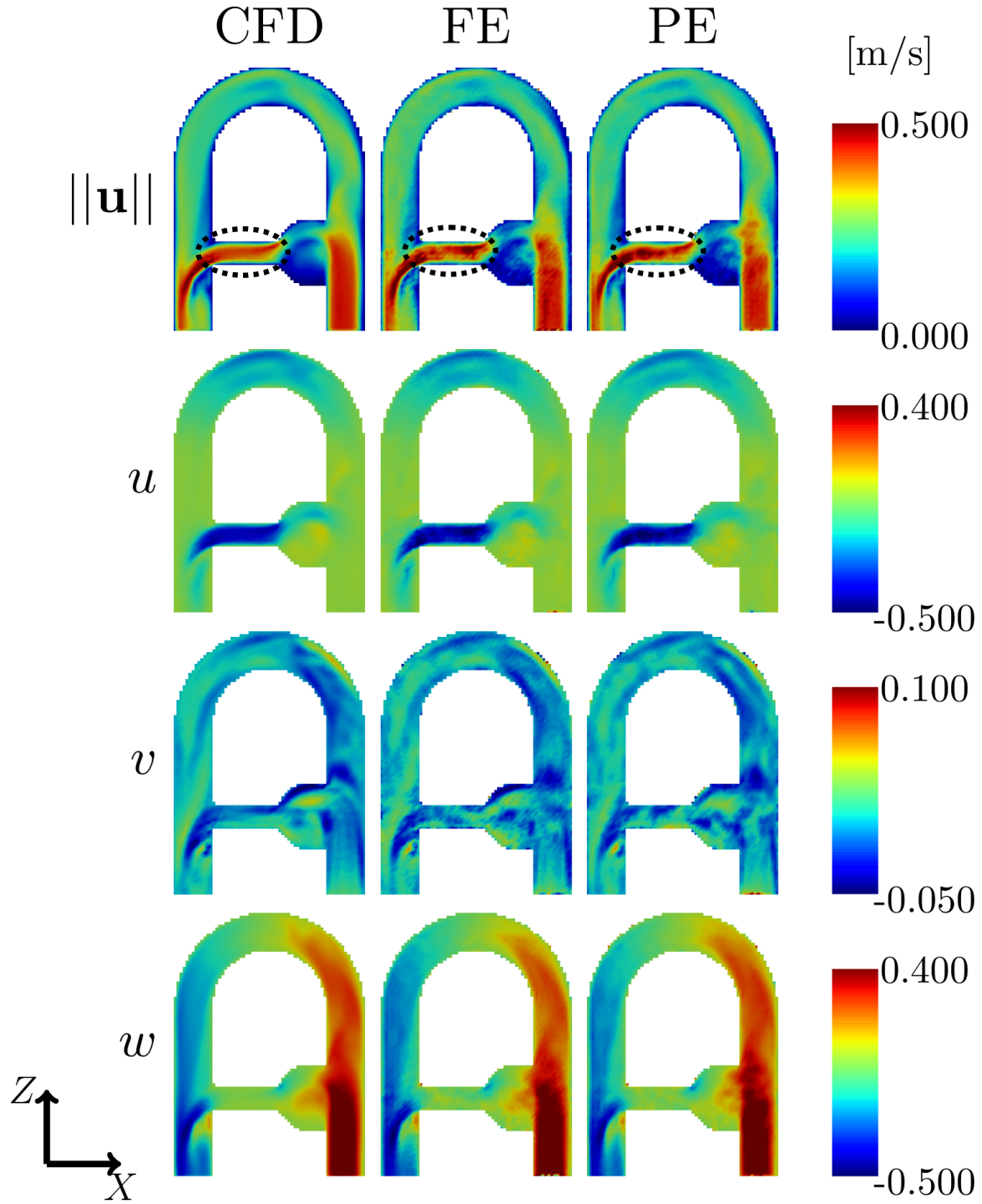


**FIGURE 3** Velocity maps for phase 0 of the sinusoidal flow rate in the coronal middle plane.  $||\vec{u}||$  is the magnitude of the velocity vector  $[u, v, w]$ . CFD stands for computational fluid dynamics, FE for full echo synthetic MRI and PE for partial echo synthetic MRI. The collateral is circled as an example of region where discrepancies between the synthetic MRI and the CFD are visually observed.

solid lines). The highest contribution to the RMSE comes from the velocity component  $w$ , which corresponds to the readout direction  $Z$  (in red, cf. Figure 2 for the axis

directions). It is this contribution, in particular, that is significantly reduced during the acquisition of synthetic MRI signal with PE. Along  $X$  (in blue) and  $Y$  (in gray),

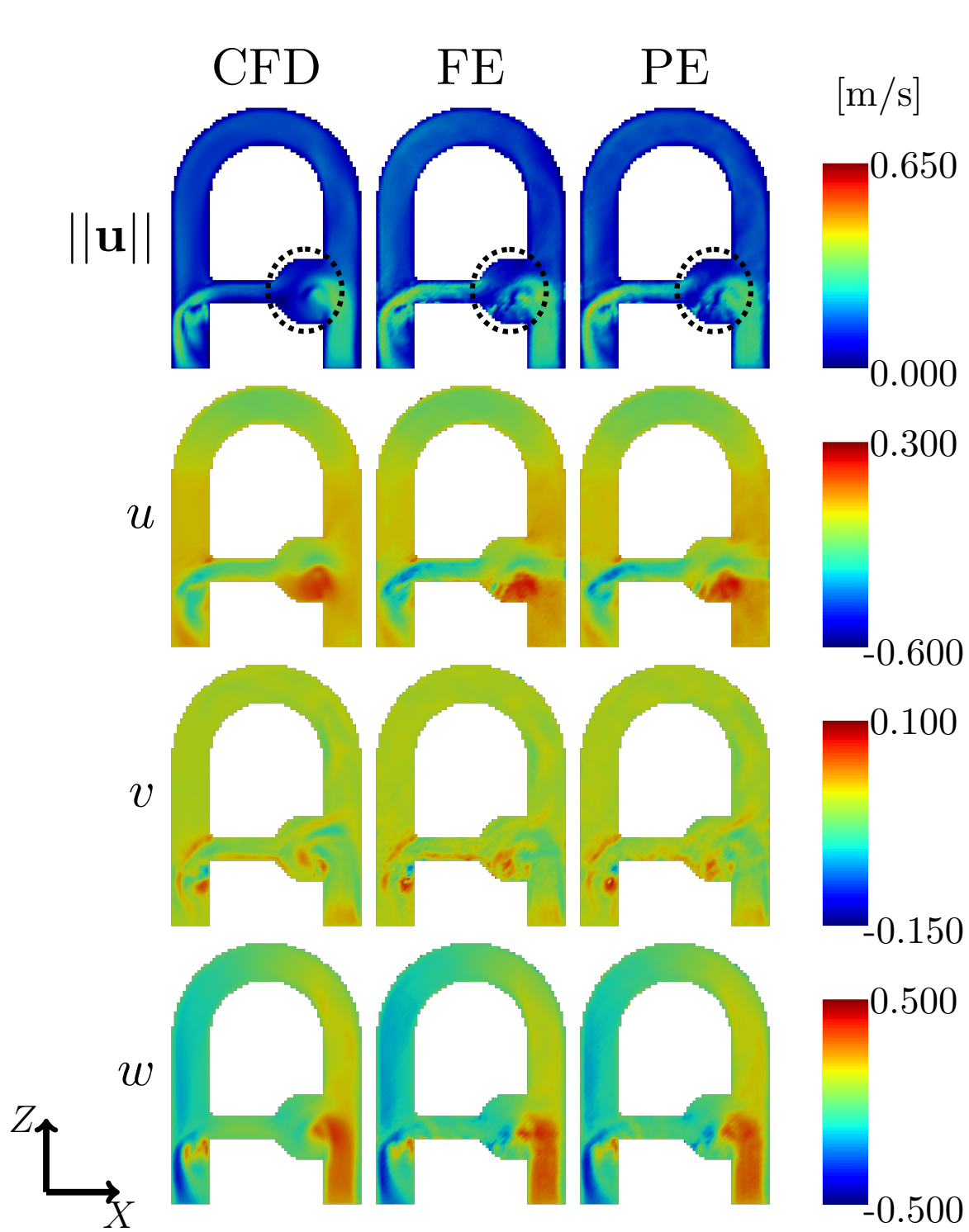


**FIGURE 4** Velocity maps for phase 10 of the physiological flow rate in the coronal middle plane.  $\|\vec{u}\|$  is the magnitude of the velocity vector  $[u, v, w]$ . CFD stands for computational fluid dynamics, FE for full echo synthetic MRI and PE for partial echo synthetic MRI. The aneurysm is circled as an example of region where discrepancies between the synthetic MRI and the CFD are visually observed.

the errors are almost not impacted by the use of PE. As expected, the lowest contribution to the average error comes from the low velocities of the velocity component

$v$ . For the physiological flow, the highest RMSE is found at phase 10, when the inlet flow is decelerating after peak systole (cf. plot on the bottom right in Figure 2).

Note that deceleration has been reported to promote flow instabilities<sup>29</sup>. Concerning the sinusoidal inlet flow rate, the highest errors are found at peak systole for the FE readout, but they are happening at phase 13 for PE. This phase is characterized by a positive flow rate at the inlet (see Figure 2), yet still backward flow in the collateral and aneurysm-like region (cf. velocity maps in Figure S3). This means that there are both an inflow coming from the inlet into the aneurysm/collateral branch and a backflow from the collateral towards the inlet. This leads to complex flow in the aneurysm and potential sign changes of the velocity components due to flow reversal in the collateral. If a sign change occurs during the time delay between velocity and spatial encodings, this would lead to incorrect mapping of the reconstructed velocities.

To shed light on the spatial structure of the errors, the error maps are presented in Figure 6 for phase 0 of the sinusoidal inflow and in Figure 7 for phase 10 of the physiological one (the same phases as in Figures 3 and 4). The error maps of the other phases are provided as Supporting Information Figures S7-12. For both inflows, with and without PE, the errors on  $v$  are relatively low as compared to the other velocity components. One exception is phase 10 for the physiological inflow, where higher error levels are noticed in the mixing layer under the jet at the junction between the collateral and the main branch. The highest errors on  $u$  are mainly located in the aneurysm and the collateral for all phases. These regions are mainly oriented along the  $X$ -axis, that is where the extrema of  $u$  are reached. Finally, the errors on  $w$  are happening in the whole geometry. The use of PE for both types of inflow reduces these errors in particular in the U-bend. This is also noticed in the global RMSE. Furthermore, high levels of RMSE are seen in the collateral and around (aneurysm and jet) when comparing any of the synthetic MRI with the corresponding CFD. However, these higher errors are not observed for the RMSE between the synthetic MRI without and with PE. This shows a relatively good agreement between the two sequences in these regions. But it also indicates that there is a discrepancy between the CFD velocity field and the ones obtained by synthetic MRI, despite those latter ones being computed based on the first one.

### 3.3 | Origins of errors inherent to the synthetic MRI procedure

As underlined in the last paragraph, PE seems to reduce the errors on  $w$  and hence the RMSE between synthetic MRI and CFD overall (cf. Figure 5). Yet, discrepancies are still present between both modalities. In an attempt to understand the origins of these errors inherent to the synthetic MRI procedure, two metrics detailed in section

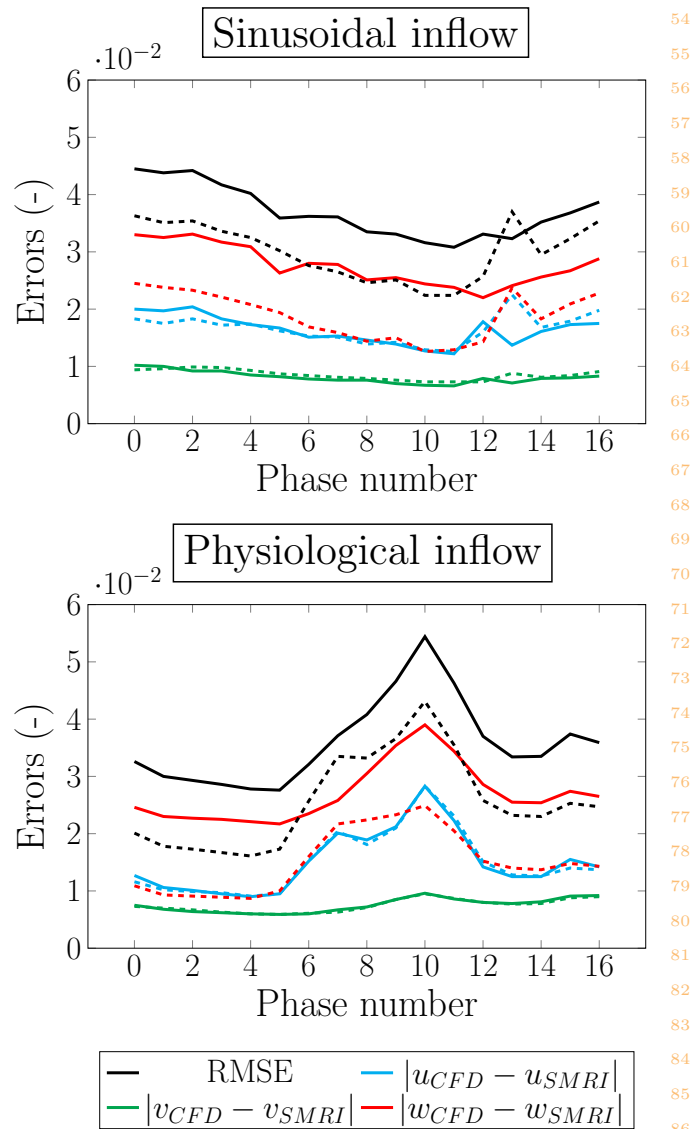


**FIGURE 5** Evolution of the absolute errors (on  $u$  in blue, on  $v$  in green and on  $w$  in red) and Root Mean Squared Errors (RMSE, in black) throughout the cardiac cycle for the sinusoidal (above) and physiological (below) inflows. The solid lines represent the acquisition with full echo, while the dashed lines represent the acquisition with partial echo. All errors are normalized by the maximal  $V_{ENC} = 0.7$  m/s.

2.5 are investigated: the norm of the acceleration  $\left\| \frac{D\vec{u}}{Dt} \right\|$  and the TKE. Thresholds on the RMSE and these metrics are displayed in Figure 8 for both inflows. The threshold for the RMSE is set to 8.2%. The quantity  $RMSE \times V_{enc}$  is homogeneous to a velocity and regions above this threshold correspond to a displacement of 3 mm (a voxel and a half) over the duration of one cardiac phase. Concerning  $\left\| \frac{D\vec{u}}{Dt} \right\|$ , the threshold corresponds to accelerations which would induce a displacement greater than a voxel over the duration of one cardiac phase. Finally, the highlighted regions for TKE are the ones

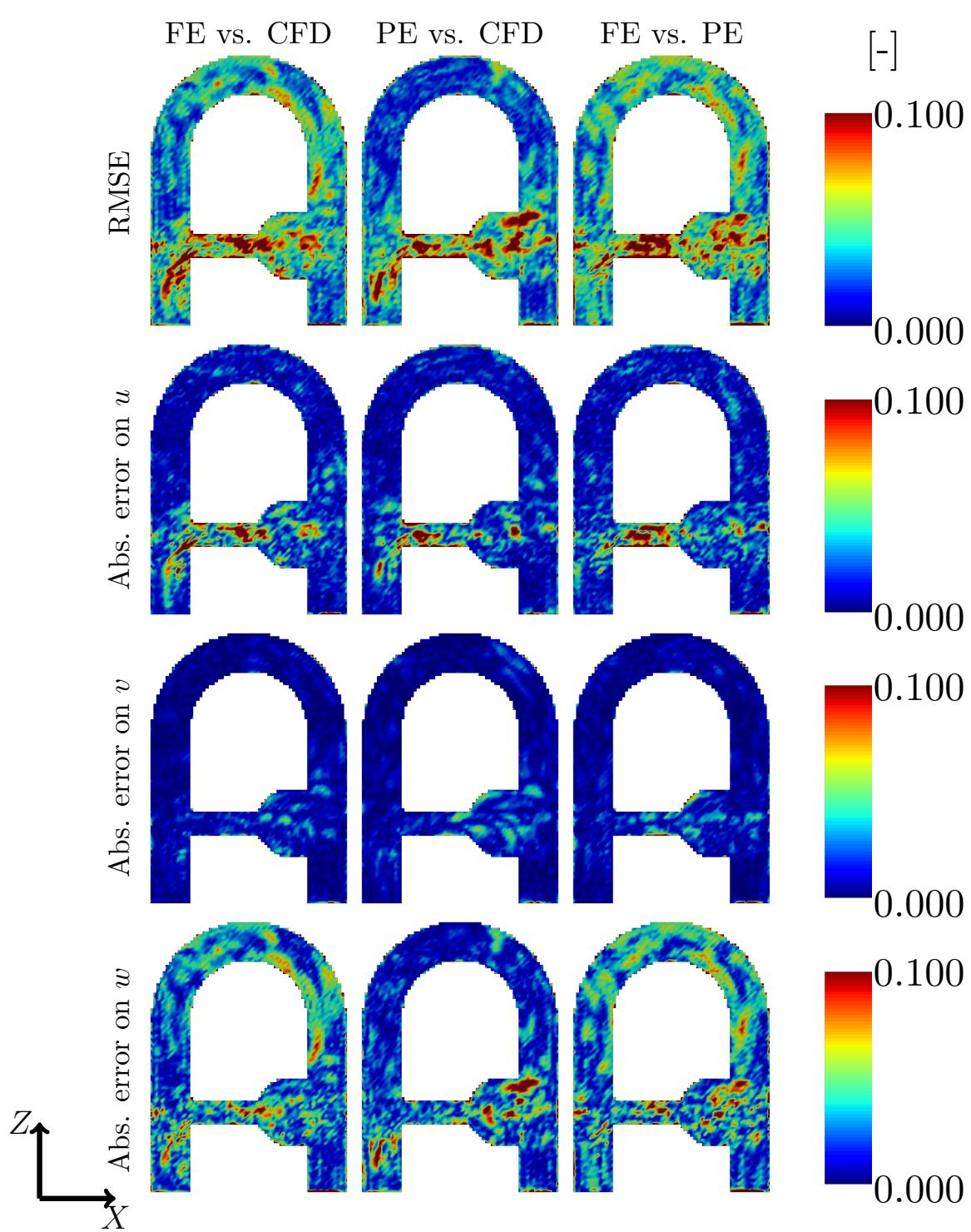


**FIGURE 6** Root Mean Squared Errors (RMSE) and absolute errors maps for phase 0 of sinusoidal flow rate. The 1<sup>st</sup> and 2<sup>nd</sup> columns compare the synthetic MRI, respectively with full echo (FE) and with partial echo (PE), against the corresponding computational fluid dynamics simulations (CFD). The last column compares both synthetic MRI fields. All errors are normalized by the maximal  $V_{ENC} = 0.7$  m/s.

above 10% of the mean kinetic energy injected at the inlet. The thresholds have been manually tuned in order to highlight similar patterns observed for the errors and the metrics.

These thresholds are displayed in Figure 8 for phase 0 of the sinusoidal inflow and phase 10 of the physiological one. Other phases are reported as Supporting

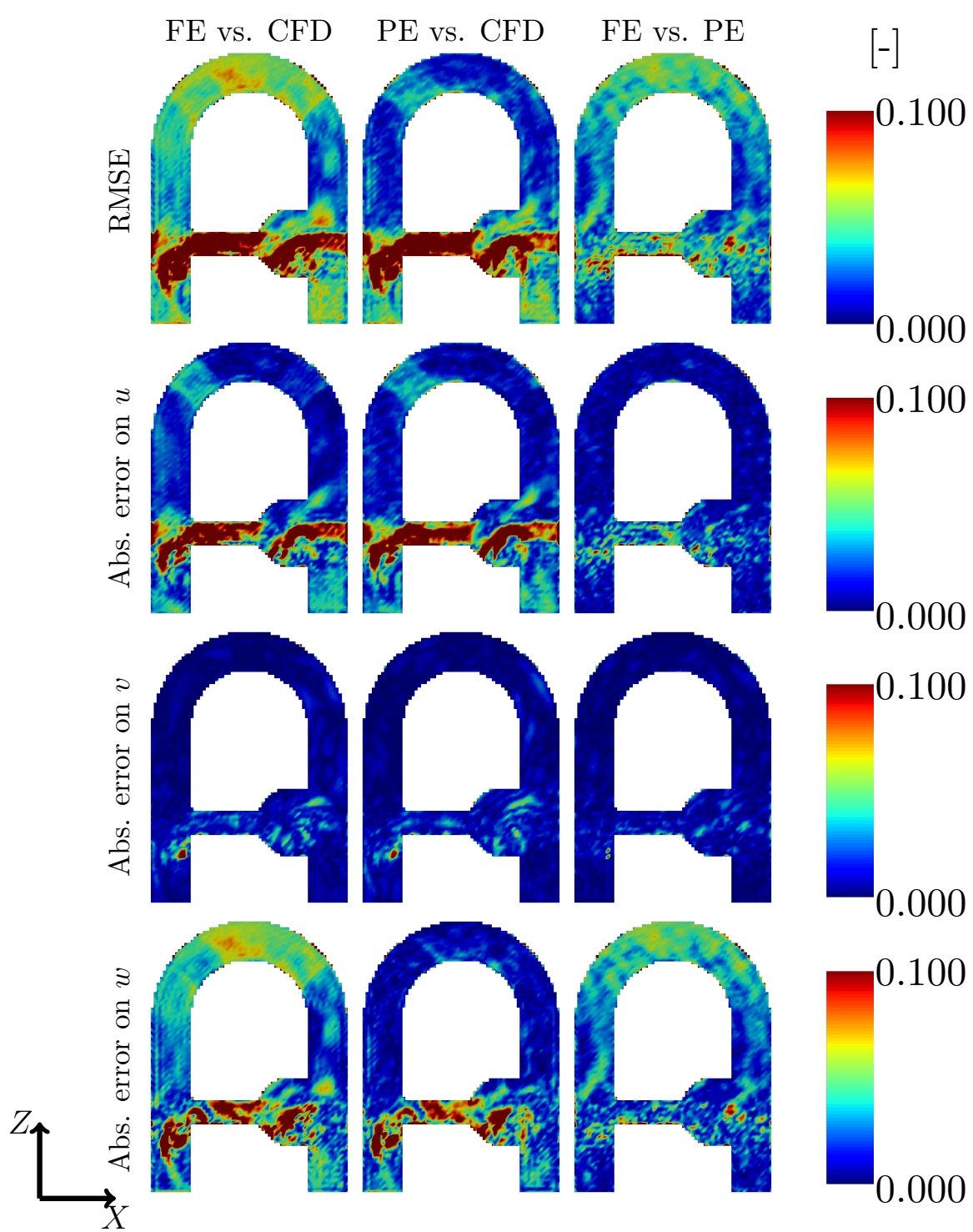


**FIGURE 7** Root Mean Squared Errors (RMSE) and absolute errors maps for phase 10 of physiological flow rate. The 1<sup>st</sup> and 2<sup>nd</sup> columns compare the synthetic MRI, respectively with full echo (FE) and with partial echo (PE), against the corresponding computational fluid dynamics simulations (CFD). The last column compares both synthetic MRI fields. All errors are normalized by the maximal  $V_{ENC} = 0.7$  m/s.

Information Figures S13-18. The RMSE maps (1st column) show that the highest levels occur mainly in the collateral (both phases presented, and see Figures S16-18 for the physiological inflow), in the aneurysm (both

phases presented, as well as phase 6 for the sinusoidal inflow in Figure S13 and phase 12 in Figure S18 for the physiological inflow) and in the jet and recirculation below when presents (both phases presented, as well as

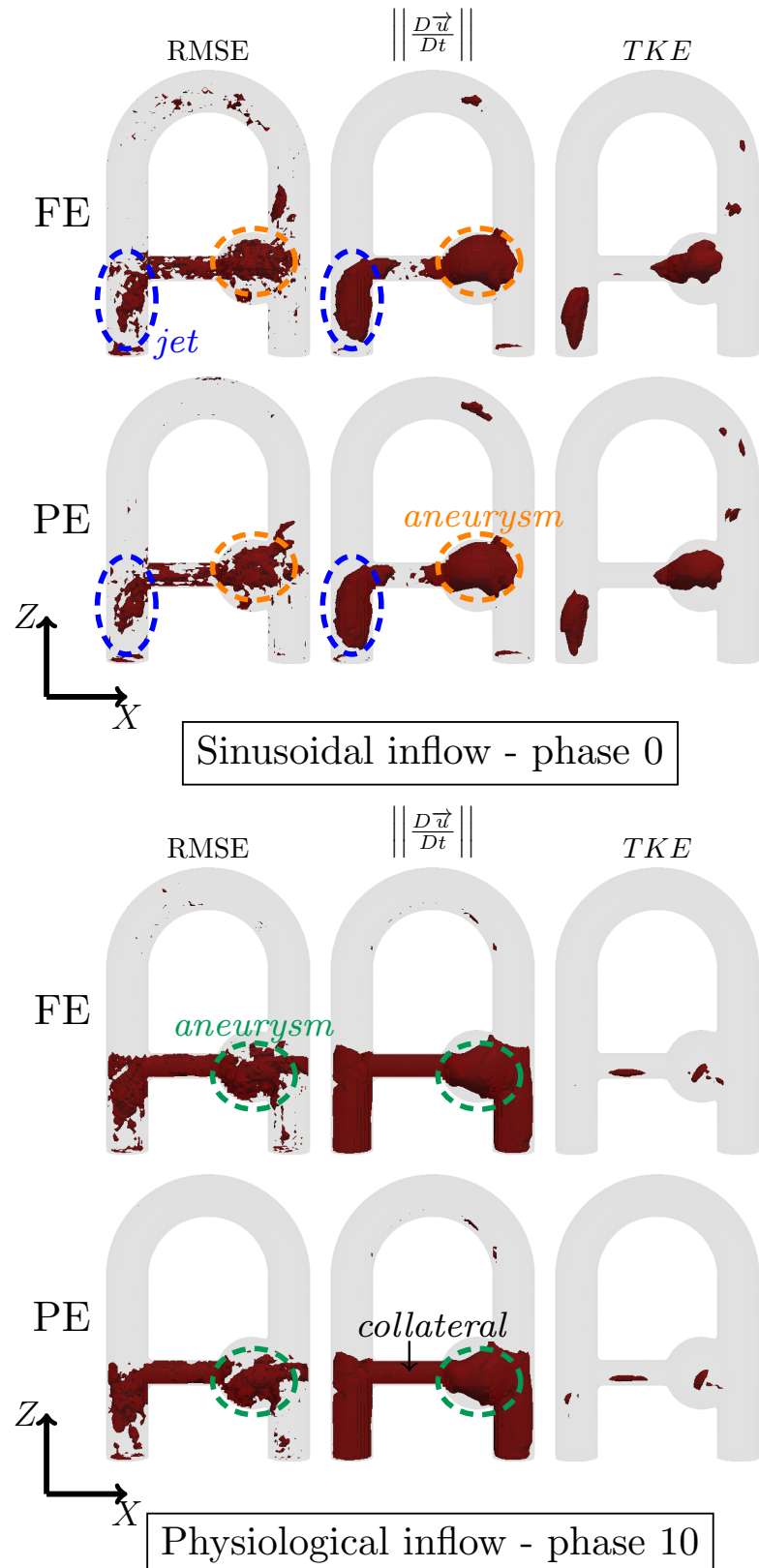


**FIGURE 8** Thresholds on the root mean square error (RMSE  $\geq 8.2\%$ ), acceleration ( $\left\| \frac{D\vec{u}}{Dt} \right\| \geq 1.48 \text{ m/s}^2$ ), and turbulent kinetic energy (TKE  $\geq 0.002 \text{ m}^2/\text{s}^2$  for the sinusoidal inflow and  $\geq 0.0008 \text{ m}^2/\text{s}^2$  for the physiological inflow). Regions with similar patterns for RMSE and acceleration are circled: in blue for the jet region and in orange for the upper part of the aneurysm in phase 0 of the sinusoidal inflow and in green the lower part of the aneurysm in phase 10 of the physiological inflow.

phase 8 in Figure S17 for the physiological inflow). The acceleration field catches numerous patterns similar to these regions of high RMSE. For example for the sinusoidal inflow, the acceleration caused by the jet (regions circled in blue in Figure 8) and in the upper part of the aneurysm (regions circled in orange in Figure 8) seems to be related to the RMSE in phase 0. Concerning the physiological inflow, the locations of high acceleration within the aneurysm are similar to the one of high RMSE for phase 10 (regions circled in green in Figure 8, see phase 12 in Figure S18, too). The high levels of TKE mainly relate to the high RMSE occurring in the aneurysm (see phases 6 and 13 for the sinusoidal inflow, respectively in Figures S13 and S15).

Of course, the metrics are not independent and their simultaneous effects impact the discrepancies between the synthetic MRI and CFD fields. One can note that regions of high acceleration, e.g. at the inlet for phase 10 of the physiological flow, do not necessarily result in a high level of error. Furthermore, some regions of high RMSE appear to be uncorrelated with the computed metrics.

## 4 | DISCUSSION AND CONCLUSIONS

The aim of this work is to investigate the use of PE in the context of 4D flow MRI. MRI-CFD simulations are conducted in a rigid flow phantom for two different pulsatile inflow signals: a sinusoidal waveform and a physiological waveform representing the ascending aorta flow rate. A FE acquisition and a PE acquisition covering 75% of the expected readout are simulated with all other parameters kept identical up to the restrictions of the sequence design software. This numerical setup allows to investigate the impact of PE on the MRI process, without experimental artifacts. Indeed, no motion of the phantom itself is simulated, nor are Maxwell terms, eddy currents or gradient nonlinearities. The reconstructed synthetic MRI velocity fields are compared to the phase-averaged and downsampled velocity fields derived from the CFD fields used to simulate the MRI process.

Qualitative comparison indicates that the synthetic MRI images are in good agreement with the CFD velocity fields across all components, for both inflow signals, with and without PE. Quantitatively, the velocity component  $w$  shows higher absolute errors for FE than for PE. On the contrary, the error levels are similar for the  $u$  and  $v$  components with both acquisitions. While  $u$  and  $v$  are encoded along phase-encoding directions,  $w$  is encoded along the frequency-encoded direction. Hence, there is an incompressible delay between the velocity and the spatial encodings along the  $Z$  direction. In

the two investigated sequences, the gradients along  $X$  (phase-encoding direction) and  $Y$  (slice-selecting direction) have the same gradient amplitudes and durations. Using PE, along the  $Z$ -axis, the readout gradient is not only shorter with same strength, but the preceding gradients (prephasing, flow-compensation and velocity-encoding) show reduced amplitudes. Consequently,  $T_D$ , the time delay between the effective encoding time and  $T_E$ , is reduced by about 25% with PE, which can be accountable for the lower errors reported on  $w^8$ . To prove that improved errors are mainly due to shortening  $T_D$ , an *artificial* PE reconstruction has been created with an echo symmetry fraction of 75% (the same as for PE). The RMSE evolution of FE, *artificial* PE and PE, for both inflows, is provided as Supporting Information Figure S19. It is observed that the RMSE levels obtained for *artificial* PE are almost identical to the ones obtained for the FE acquisitions they are based on. It provides insights that the differences between FE and PE are not due to k-space undersampling.

Maps of errors between the synthetic MRI and the reference CFD data were discussed. As the simulations assume an ideal MRI framework, errors are necessarily related to the intrinsic limitations of PC-MRI measurement. First, RMSE maps are shown to be similar to the acceleration maps. Indeed, PC-MRI relies on the assumption that flow velocity changes slowly compared to the temporal resolution. Velocity is then considered to be constant and higher-order terms (acceleration, jerk etc.) are neglected<sup>9</sup>. Yet, even in the context of steady flow, fluid elements may be accelerated in complex geometries, e.g. in stenoses or curved vessels<sup>30,31</sup>, due to their transport in a non-uniform velocity field. Furthermore, when handling pulsatile flows as in the aorta, the time dependence of velocity cannot be neglected. For basic purely anatomical GRE sequences the temporal resolution matches the repetition time  $T_R$ . Here, the common 4-point encoding scheme used in the present work results in a 4-fold increase in acquisition time multiplied by the number of segments per point. Given the phantom's complex geometry and the pulsatile inflow conditions, the constant velocity assumption yields substantial errors.

According to the TKE values, turbulence occurs mainly in the aneurysm-like region (see Supporting Information Figures S13 and S15). TKE appears as complementary to the acceleration to understand the RMSE. Note that this quantity could not be assessed based on the intravoxel spin velocity standard deviation (IVSD) method proposed by Dyverfeldt et al.<sup>32,33,28</sup> due to the symmetric 4-point encoding scheme used in this study. This scheme leads to the same first gradient moments for each segment, which is the only restriction in the use

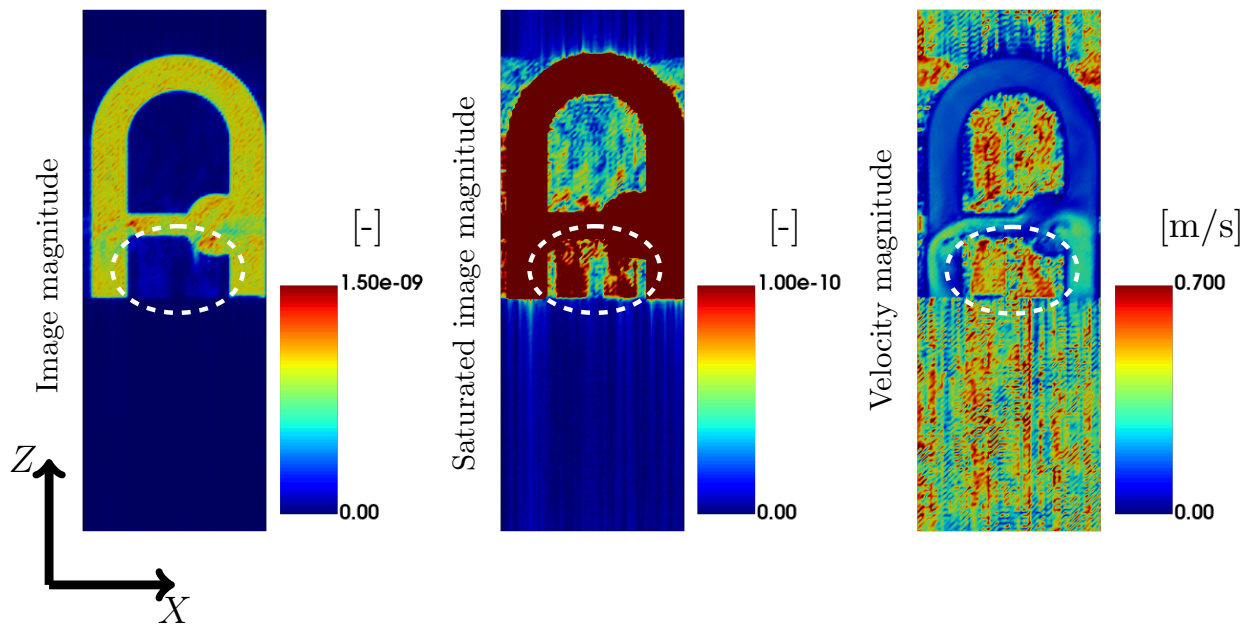


**FIGURE 9** Ghosting artifact as seen on magnitude images and velocity magnitude for phase 10 of the physiological inflow. While only one phantom geometry is observed in the image magnitude (left), the saturated image magnitude reveals a duplicate mainly of the inlet and outlet (see circled region). This phase corresponding to the highest deceleration of the flow rate is particularly affected by these artifacts, which could impact the velocity field as well.

of this method. An asymmetric 4-point encoding scheme could be investigated in a future work to evaluate this computation of TKE.

Some RMSE regions remain unexplained by the proposed metrics, e.g. in the aneurysm-like region and its prolongation above the inlet in phase 10 for the physiological inflow (see phase 6 in Figure S16, too). The errors in this area could be related to the ghosting artifact. The magnitude images for phase 10, as well as the velocity magnitude field, are displayed in Figure 9. The same images are provided for phases 6 and 12 in Supporting Information Figures S20-21, where the latter phase gives an example free of ghosting. At first sight, only the expected phantom geometry is observed in the image magnitude. However, saturating the signal intensity reveals one replicate more visible in phases 6 and 10. The inlet and outlet are especially highlighted in the magnitude images. The fact that the replicate propagates along the phase-encoding axis indicates that it is due to an inter-view motion, occurring on a timescale longer than  $T_R$ <sup>34</sup>. Since two copies of the phantom are noticed, it is likely that the ghosting is related to the fact that two segments are encoded per cardiac phase in the sequences of this study. That means that for a given velocity direction and for a given phase, every odd line of the k-space is collected during the first part of their cardiac phase and every even line during the second part of the cardiac phase. With the periodic pulsatile inflow,

this results in every other line not being collected at the same time instant with respect to the cardiac cycle. This creates coherent phase-shifting in the acquired k-space<sup>34,35</sup>, which is exacerbated when there is a larger difference in the inflow between the first and second part of the cardiac phase considered.

The limitations of this study warrant caution in generalizing the results to a clinical context. Although more realistic than the sequences used in the preliminary study conducted by Puiseux et al.<sup>17</sup>, the sequences remain idealized in several respects. First, a numerical perfect spoiling is performed instead of being simulated. Furthermore, the frequency of the pulsatile inflow is perfectly matched to the prospective sequence, which does not allow for the consideration of irregular heartbeats. While their absence makes it possible to distinguish sources of errors which only arise from the sequence and the MR process in itself, gradient field distortions (e.g., eddy currents<sup>2</sup>, gradient nonlinearities<sup>36</sup>) could be modeled to investigate their impact on the reconstructed velocity fields. Noise could be added as well to the synthetic MRI k-spaces to study its effect on the reconstructed images.

In order to achieve a reasonable computing time, a coarse mesh has been used with a characteristic cell size of 2 mm. It would be of interest to conduct additional simulations with finer spatial resolutions. Yet, the CFD resolution used is still below the synthetic MRI resolution, which should mitigate the errors. Furthermore,

the spin density exceeds the recommendation of 3 particles/direction/voxel to keep an error on the MR signal below 1.5%<sup>37</sup>. Another limitation of the flow phantom is its rigid walls. Studying a geometry with moving walls and thereby with properties closer to the walls of the aorta or the heart muscle would be of interest to assess the impact of motion artifacts on the reconstructed velocity fields. Bulk or cyclic motion of the phantom could be implemented to mimic patient motion. Other geometries could be investigated as well such as stenoses or patient-specific geometries. This would provide more insights on clinical applicability.

The present study could be expanded by investigating other strategies to fill the k-space. If filled in a Cartesian manner, different interleaved patterns could be investigated, as well as asymmetric encoding scheme for the velocity-encoding. A natural follow-up of our numerical pipeline would be to investigate new sequences, such as the one proposed by Bruschewski et al. where a synchronization of all encoding time points is achieved to mitigate misregistration<sup>38</sup>. Additionally, the framework has the potential to simulate radial<sup>39,40</sup> or spiral<sup>41,42</sup> samplings. Besides, this study focuses on the impact of a single parameter but opens the possibility for future investigations into other factors, such as resolution, readout bandwidth, or  $V_{ENC}$ , as well as their combined effects on the reconstructed flow fields.

In summary, the MRI-CFD framework used in this work appears as a useful tool to investigate the design of 4D flow MRI sequences. This framework allowed to show strong evidence that PE provides better outcomes than FE in a well-controlled phantom exhibiting a flow pattern typical of that observed in large arteries. In this specific context, the reduction of the displacement artifacts have more impact on the reconstructed velocity fields than the missing k-space data. From another perspective, the framework proved its ability to reproduce artifacts inherent to the 4D flow MRI process. Thereby, these realistic synthetic 4D flow data could be used as input datasets to train machine learning models and physics-informed neural networks<sup>43,44,45</sup>. The synthetic MRI k-spaces could as well be of interest as input for to test reconstruction algorithms or to build new reconstruction methods.

## ACKNOWLEDGMENTS

Simulations with YALES2BIO were performed using HPC resources from GENCI-CINES (grant numbers A0120312498 and A0140312498) and with the support of the MESO@LR-Platform at the University of Montpellier.

## DATA AVAILABILITY STATEMENT

Except for the sequence files, the data that support the findings of this study are available upon request, which include among other the CFD solutions, the reconstruction scripts and the reconstructed synthetic MRI images. The data are not publicly available due to issues on public storage of large files. The pseudo-code of the MRI-CFD simulation procedure has been published in<sup>17</sup>.

## Conflict of interest

### ORCID

Morgane Garreau	 0000-0001-8242-6539
Thomas Puiseux	 0000-0002-3548-6085
Ramiro Moreno	 0000-0002-1702-1380
Solenn Toupin	 0000-0001-9967-0044
Daniel Giese	 0000-0002-3925-4441
Franck Nicoud	 0000-0002-0006-8422
Simon Mendez	 0000-0002-0863-2024

## REFERENCES

- Bissell Malenka M., Raimondi Francesca, Ait Ali Lamia, et al. 4D Flow cardiovascular magnetic resonance consensus statement: 2023 update. *Journal of Cardiovascular Magnetic Resonance*. 2023;25(1):40.
- Bernstein Matt A., King Kevin F., Zhou Xiaohong Joe. *Handbook of MRI Pulse Sequences*. Academic Press; 1 ed.2004.
- Noll D.C., Nishimura D.G., Macovski A.. Homodyne detection in magnetic resonance imaging. *IEEE Transactions on Medical Imaging*. 1991;10(2):154–163.
- Liang Zhi-Pei, Boada Fernando E., Constable R. Todd, Haacke E. Mark, Lauterbur Paul C., Smith Michael R.. Constrained Reconstruction Methods in MR Imaging. *Reviews of Magnetic Resonance in Medicine*. 1992;4:67–185.
- McGibney G., Smith M. R., Nichols S. T., Crawley A.. Quantitative evaluation of several partial fourier reconstruction algorithms used in mri. *Magnetic Resonance in Medicine*. 1993;30(1):51–59.
- Steinman David A., Ethier C. Ross, Rutt Brian K.. Combined analysis of spatial and velocity displacement artifacts in phase contrast measurements of complex flows. *Journal of Magnetic Resonance Imaging*. 1997;7(2):339–346.
- Evans Avery J, Richardson Donna B, Tien Robert, et al. Poststenotic Signal Loss in MR Angiography: Effects of Echo Time, Flow Compensation, and Fractional Echo. *AJNR*. 1993;14(721-729).
- Thunberg Per, Wigström Lars, Ebbers Tino, Karlsson Matts. Correction for displacement artifacts in 3D phase contrast imaging. *Journal of Magnetic Resonance Imaging*. 2002;16(5):591–597.

- 01 9. Markl Michael. *Velocity Encoding and Flow Imaging*. 05.
- 02 10. Urchuk Steven N., Plewes Donald B.. Mechanisms of 04 flow-induced signal loss in MR angiography. *Journal of Magnetic Resonance Imaging*. 1992;2(4):453–462.
- 03 11. Frayne Richard, Rutt Brian K.. Understanding 06 acceleration-induced displacement artifacts in phase-contrast MR velocity measurements. *Journal of Magnetic Resonance Imaging*. 1995;5(2):207–215.
- 04 12. Zhong Liang, Schrauben Eric M., Garcia Julio, et al. 07 Intracardiac 4D Flow MRI in Congenital Heart Disease: Recommendations on Behalf of the ISMRM Flow & Motion Study Group. *Journal of Magnetic Resonance Imaging*. 2019;50(3):677–681.
- 05 13. Weine Jonathan, McGrath Charles, Dirix Pietro, Buoso 09 Stefano, Kozerke Sebastian. CMRsim –A python package 11 for cardiovascular MR simulations incorporating complex motion and flow. *Magnetic Resonance in Medicine*. 2024;91(6):2621–2637.
- 06 14. Klepaczko Artur, Materka Andrzej, Szczypinski Piotr, 13 Strzelecki Michal. Numerical Modeling of MR Angiography for Quantitative Validation of Image-Driven Assessment of Carotid Stenosis. *IEEE Transactions on Nuclear Science*. 2015;62(3):619–627.
- 07 15. Klepaczko Artur, Szczypinski Piotr, Strzelecki Michal, 15 Stefanczyk Ludomir. Simulation of phase contrast angiography for renal arterial models. *BioMedical Engineering OnLine*. 2018;17(1):41.
- 08 16. Puiseux Thomas, Sewonu Anou, Meyrignac Olivier, et al. 17 Reconciling PC-MRI and CFD: An in-vitro study. *NMR in Biomedicine*. 2019;32(5):e4063.
- 09 17. Puiseux Thomas, Sewonu Anou, Moreno Ramiro, 19 Mendez Simon, Nicoud Franck. Numerical simulation of 21 time-resolved 3D phase-contrast magnetic resonance imaging. *PLOS ONE*. 2021;16(3):e0248816.
- 10 18. Garreau Morgane, Puiseux Thomas, Toupin Solenn, et al. 23 Accelerated sequences of 4D flow MRI using GRAPPA and 25 compressed sensing: A comparison against conventional MRI and computational fluid dynamics. *Magnetic Resonance in Medicine*. 2022;88(6):2432–2446.
- 11 19. Stevens Scott A., Lakin William D., Goetz Wolfgang. A 27 differentiable, periodic function for pulsatile cardiac output based on heart rate and stroke volume. *Mathematical Biosciences*. 2003;182(2):201–211.
- 12 20. Pelc Norbert J., Bernstein Matt A., Shimakawa Ann, 29 Glover Gary H.. Encoding strategies for three-direction 31 phase-contrast MR imaging of flow. *Journal of Magnetic Resonance Imaging*. 1991;1(4):405–413.
- 13 21. Markl Michael, Frydrychowicz Alex, Kozerke Sebastian, 33 Hope Mike, Wieben Oliver. 4D flow MRI. *Journal of Magnetic Resonance Imaging*. 2012;36(5):1015–1036.
- 14 22. Mendez Simon, Bérod Alain, Chnafa Christophe, et al. 35 YALES2BIO: A General Purpose Solver Dedicated to Blood Flows. In: John Wiley & Sons, Ltd 2022 (pp. 183–206).
- 15 23. Moyle Keri R., Antiga Luca, Steinman David A.. Inlet 37 Conditions for Image-Based CFD Models of the Carotid Bifurcation: Is it Reasonable to Assume Fully Developed Flow?. *Journal of Biomechanical Engineering*. 2006;128(3):371–379.
- 16 24. Szarf Gilberto, Dori Yoav, Rettmann Dan, et al. Zero 39 filled partial fourier phase contrast MR imaging: In vitro 41 and in vivo assessment. *Journal of Magnetic Resonance Imaging*. 2006;23(1):42–49.
- 17 25. Walheim Jonas, Kozerke Sebastian. *On Partial Fourier 43 Acquisition in 4D Flow MRI of Mean Velocities and 45 Turbulent Kinetic Energy*. 2017.
- 18 26. O'Brien Kieran R., Cowan Brett R., Jain Manali, 47 Stewart Ralph A.H., Kerr Andrew J., Young Alistair A.. 49 MRI phase contrast velocity and flow errors in turbulent 51 stenotic jets. *Journal of Magnetic Resonance Imaging*. 2008;28(1):210–218.
- 19 27. Petersson Sven, Dyverfeldt Petter, Gårdhagen Roland, 53 Karlsson Matts, Ebbers Tino. Simulation of phase 55 contrast MRI of turbulent flow. *Magnetic Resonance in Medicine*. 2010;64(4):1039–1046.
- 20 28. Ziegler Magnus, Lantz Jonas, Ebbers Tino, Dyverfeldt 57 Petter. Assessment of turbulent flow effects on the vessel 59 wall using four-dimensional flow MRI: Turbulent Flow Effects on Vessel Wall. *Magnetic Resonance in Medicine*. 2017;77(6):2310–2319.
- 21 29. Chnafa C., Mendez S., Nicoud F.. Image-Based Simulations Show Important Flow Fluctuations in a Normal 61 Left Ventricle: What Could be the Implications?. *Annals of Biomedical Engineering*. 2016;44(11):3346–3358.
- 22 30. Oshinski John N., Ku David N., Bohning Daryl E., Pettigrew Roderic I.. Effects of acceleration on the accuracy 65 of MR phase velocity measurements. *Journal of Magnetic Resonance Imaging*. 1992;2(6):665–670.
- 23 31. Dillinger Hannes, Walheim Jonas, Kozerke Sebastian. On 67 the limitations of echo planar 4D flow MRI. *Magnetic Resonance in Medicine*. 2020;84(4):1806–1816.
- 24 32. Dyverfeldt Petter, Gårdhagen Roland, Sigfridsson 69 Andreas, Karlsson Matts, Ebbers Tino. On MRI turbulence 71 quantification. *Magnetic Resonance Imaging*. 2009;27(7):913–922.
- 25 33. Casas Belen, Lantz Jonas, Dyverfeldt Petter, Ebbers 73 Tino. 4D Flow MRI-based pressure loss estimation in 75 stenotic flows: Evaluation using numerical simulations. *Magnetic Resonance in Medicine*. 2016;75(4):1808–1821.
- 26 34. Hoff Michael N., Andre Jalal B., Stewart Brent K.. Artifacts in Magnetic Resonance Imaging. In: Saba Luca, ed. *Image Principles, Neck, and the Brain*, CRC Press 77 1st ed.2016 (pp. 165–190).
- 27 35. Jou L.-D., Berger S.A.. Numerical Simulation of the Flow 79 in the Carotid Bifurcation. *Theoretical and Computational Fluid Dynamics*. 1998;10(1-4):239–248.
- 28 36. Markl M., Bammer R., Alley M.T., et al. Generalized 81 reconstruction of phase contrast MRI: Analysis and correction of the effect of gradient field distortions. *Magnetic Resonance in Medicine*. 2003;50(4):791–801.
- 29 37. Fortin Alexandre, Salmon Stéphanie, Baruthio Joseph, 83 Delbany Maya, Durand Emmanuel. Flow MRI simulation 85 in complex 3D geometries: Application to the cerebral venous network. *Magnetic Resonance in Medicine*. 2018;80(4):1655–1665.
- 30 38. Bruschewski Martin, Kolkmann Hanna, John Kristine, 87 Grundmann Sven. Phase-contrast single-point imaging 89 with synchronized encoding: a more reliable technique 91 for in vitro flow quantification. *Magnetic Resonance in Medicine*. 2006;55(4):1033–1039.

- 01      *Medicine.* 2019;81(5):2937–2946. 54
- 02      39. Feng Li. Golden-Angle Radial MRI: Basics, Advances, 55  
03      and Applications. *Journal of Magnetic Resonance Imaging.* 56  
04      2022;56(1):45–62. 57
- 05      40. Untenberger Markus, Tan Zhengguo, Voit Dirk, et al. 58  
06      Advances in real-time phase-contrast flow MRI using 59  
07      asymmetric radial gradient echoes: Real-Time Phase- 60  
08      Contrast Flow MRI. *Magnetic Resonance in Medicine.* 61  
09      2016;75(5):1901–1908. 62
- 10      41. Delattre Bénédicte M.A., Heidemann Robin M., 63  
11      Crowe Lindsey A., Vallée Jean-Paul, Hyacinthe Jean- 64  
12      Noël. Spiral demystified. *Magnetic Resonance Imaging.* 65  
13      2010;28(6):862–881. 66
- 14      42. Dyvorne Hadrien, Knight-Greenfield Ashley, Jajamovich 67  
15      Guido, et al. Abdominal 4D Flow MR Imaging in 68  
16      a Breath Hold: Combination of Spiral Sampling and 69  
17      Dynamic Compressed Sensing for Highly Accelerated 70  
18      Acquisition. *Radiology.* 2015;275(1):245–254. 71
- 19      43. Fathi Mojtaba F., Perez-Raya Isaac, Baghaie 72  
20      Ahmadreza, et al. Super-resolution and denoising of 73  
21      4D-Flow MRI using physics-Informed deep neural 74  
22      nets. *Computer Methods and Programs in Biomedicine.* 75  
23      2020;197:105729. 76
- 24      44. Karniadakis George Em, Kevrekidis Ioannis G., Lu Lu, 77  
25      Perdikaris Paris, Wang Sifan, Yang Liu. Physics- 78  
26      informed machine learning. *Nature Reviews Physics.* 79  
27      2021;3(6):422–440. 80
- 28      45. Ferdian Edward, Dubowitz David J., Mauger Charlene A., Wang Alan, Young Alistair A.. WSSNet: Aortic 81  
29      Wall Shear Stress Estimation Using Deep Learning on 82  
30      4D Flow MRI. *Frontiers in Cardiovascular Medicine.* 83  
31      2022;8:769927. 84
- 32      **How to cite this article:** Garreau M., T. Puiseux, 85  
33      R. Moreno, S. Toupin, D. Giese, S. Mendez, and F. 86  
34      Nicoud (2025), Impact of the partial echo on synthetic 87  
35      4D flow MRI sequences, *Magn. Reson. Med.*, 88  
36      Added at production. 89
- 37      90
- 38      91
- 39      92
- 40      93
- 41      94
- 42      95
- 43      96
- 44      97
- 45      98
- 46      99
- 47      100
- 48      101
- 49      102
- 50      103
- 51      104
- 52      105
- 53      106